ELSEVIER

Comput. Methods Appl. Mech. Engrg. 190 (2000) 373–386

Computer methods in applied mechanics and engineering

www.elsevier.com/locate/cma

Parachute fluid–structure interactions: 3-D computation

Keith Stein [a,*], Richard Benney [a], Vinay Kalro [b], Tayfun E. Tezduyar [b], John Leonard [c], Michael Accorsi [c]

[a] *US Army Soldier Systems Command, Natick Research, Development and Engineering Center Natick, MA, USA*
[b] *Army HPC Research Center, Minneapolis, MN, USA*
[c] *Department of Civil and Environmental Engineering, University of Connecticut, Storrs, CN, USA*

Received 20 April 1998; received in revised form 1 June 1998

Abstract

We present a parallel computational strategy for carrying out 3-D simulations of parachute fluid–structure interaction (FSI), and apply this strategy to a round parachute. The strategy uses a stabilized space-time finite element formulation for the fluid dynamics (FD), and a finite element formulation derived from the principle of virtual work for the structural dynamics (SD). The fluid–structure coupling is implemented over compatible surface meshes in the SD and FD meshes. Large deformations of the structure are handled in the FD mesh by using an automatic mesh moving scheme with remeshing as needed.

1. Introduction

In general, parachute systems are deployed from a variety of aircraft under many different conditions. All these systems deploy a deceleration device. This device is usually made of highly deformable fabrics, and it must decelerate the payload to a survivable velocity before ground impact. Fluid–structure interactions (FSI) are involved at all stages of airdrop systems performance, including at initial deployment, during inflation, at terminal descent (or gliding/maneuvering for steerable parachutes), and at soft landing (i.e., retraction for round parachutes, flared landing for ram-air parachutes). The interaction between the parachute system and the surrounding flow field is dominant in most parachute operations, and thus the ability to predict parachute FSI is of high interest to the US Army [1,2].

The dynamics of parachute systems are rather complex and difficult to model. They are governed by a nonlinear coupling between the structural dynamics of a highly deformable parachute system and the turbulent, time-dependent flow field surrounding the parachute. Recent advances in high-performance computing methods and hardware are making 3-D flow simulations and coupled fluid–structure computations for parachutes more feasible [3].

We are developing a parallel computational strategy for 3-D simulations of parachute FSI. The initial results from application to a round parachute have been obtained. The FSI strategy consists of three components: the fluid dynamics (FD) solution, the structural dynamics (SD) solution, and the coupling of the FD and SD along the fluid–structure interface.

The FD solution utilizes a stabilized space-time finite element formulation [4,5] of the time-dependent, 3-D Navier–Stokes equations. A zero-equation Smagorinsky turbulence model [6] is combined with the

* Corresponding author. Tel.: +1-508-233-5079; fax: +1-508-233-5000.
E-mail address: Keith.Stein@natick.army.mil (K. Stein).

0045-7825/00/$ - see front matter
PII: S0045-7825(00)00208-5

Navier–Stokes equations. The flow problem is discretized with an unstructured finite element mesh generator [7] to allow effective meshing of the spatial domain as the parachute shape changes in time. For the SD solution, the equations of motion for the parachute system are solved using a finite element formulation derived from the principle of virtual work for a "tension structure" composed of cables and membranes [8]. The coupling of the FD with the SD is implemented over the fluid–structure interface, which is the parachute canopy surface. For FD and SD meshes with compatible sets of nodes defining the parachute surface, the coupling involves transfer of necessary information between FD and SD surface nodes. For incompatible FD and SD meshes, coupling information must be computed with a more sophisticated projection algorithm [9]. To handle the FD mesh as the parachute undergoes large deformations, an automatic mesh moving scheme [10] with occasional remeshing of the spatial domain is being used. This coupling approach has already been demonstrated on simulation of an axisymmetric parachute inflation [11].

2. Governing equations

2.1. Fluid dynamics

Let $\Omega_t \subset \mathbb{R}^{n_{\mathrm{sd}}}$ and $(0,T)$ be the spatial and temporal domains, respectively, where n_{sd} is the number of space dimensions, and let Γ_t denote the boundary of Ω_t. The subscript t implies the time-dependence of the spatial domain. The spatial and temporal coordinates are denoted by $\mathbf{x} = (x,y,z)$ and $t \in (0,T)$. The Navier–Stokes equations for incompressible flows are

$$\rho\left(\frac{\partial \mathbf{u}}{\partial t} + \mathbf{u}\cdot\nabla\mathbf{u} + \mathbf{f}\right) - \nabla\cdot\boldsymbol{\sigma} = \mathbf{0} \quad \text{on } \Omega_t, \tag{1}$$

$$\nabla\cdot\mathbf{u} = 0 \quad \text{on } \Omega_t, \tag{2}$$

where ρ is constant density and $\mathbf{u} = (u,v,w)$ is the velocity vector. Here $\mathbf{f}$ is an external force term consisting of gravity. For the Newtonian fluids under consideration, the stress tensor for a fluid with dynamic viscosity μ is defined as follows:

$$\boldsymbol{\sigma}(\mathbf{u},p) = -p\mathbf{I} + 2\mu\boldsymbol{\varepsilon}(\mathbf{u}), \tag{3}$$

where $\boldsymbol{\varepsilon}(\mathbf{u})$ is the strain rate tensor.

$$\boldsymbol{\varepsilon}(\mathbf{u}) = \frac{1}{2}\left(\nabla\mathbf{u} + (\nabla\mathbf{u})^{\mathrm{T}}\right). \tag{4}$$

Both the Dirichlet and Neumann-type boundary conditions are accounted for, represented as

$$\begin{aligned} \mathbf{u} &= \mathbf{g} \quad \text{on } (\Gamma_t)_g, \\ \mathbf{n}\cdot\boldsymbol{\sigma} &= \mathbf{h} \quad \text{on } (\Gamma_t)_h, \end{aligned} \tag{5}$$

where $(\Gamma_t)_g$ and $(\Gamma_t)_h$ are complementary subsets of the boundary Γ_t. The initial condition on the velocity is specified as $\mathbf{u}(\mathbf{x},0) = \mathbf{u}_0$ on Ω_0, where $\mathbf{u}_0$ is divergence free. For the problems under consideration, the μ is modified locally using a Smagorinsky turbulence model and is replaced by an "effective" turbulent viscosity μ_{t} as follows:

$$\mu_{\mathrm{t}} = \mu + (\kappa h_{\mathrm{e}})^2\sqrt{2\boldsymbol{\varepsilon}(\mathbf{u}) : \boldsymbol{\varepsilon}(\mathbf{u})}, \tag{6}$$

where $\kappa = 0.15$, and h_{e} is a measure of the element length.

2.2. Structural dynamics

Let $\Omega_t^{\mathrm{s}} \subset \mathbb{R}^{n_{\mathrm{sd}}}$ be the spatial domain bounded by Γ_t^{s}. The boundary Γ_t^{s} is composed of $(\Gamma_t^{\mathrm{s}})_g$ and $(\Gamma_t^{\mathrm{s}})_h$. The equations of motion for the structural system are

$$\rho^s\left(\frac{\mathrm{d}^2\mathbf{y}}{\mathrm{d}t^2}-\mathbf{f}\right)-\nabla\cdot\boldsymbol{\sigma}^s=\mathbf{0}\quad\text{on }\Omega_t^s, \tag{7}$$

where, $\mathbf{y}$ is the displacement vector, ρ^s is the material density, $\mathbf{f}$ are the external body forces acting on the structure, and $\boldsymbol{\sigma}^s$ is the Cauchy stress tensor. The Cauchy stress tensor $\boldsymbol{\sigma}^s$ and the Piola–Kirchoff stress tensor $\mathbf{S}$ are related through a geometric transformation. For Hookean materials with linear-elastic properties, under the assumption of large displacements with small strains, $\mathbf{S}$ for membranes become,

$$\begin{aligned}
S^{ij}&=\left(\bar{\lambda}_{\mathrm{m}}G^{ij}G^{kl}+\mu_{\mathrm{m}}\left[G^{il}G^{jk}+G^{ik}G^{jl}\right]\right)E_{kl},\\
\bar{\lambda}_{\mathrm{m}}&=\frac{2\lambda_{\mathrm{m}}\mu_{\mathrm{m}}}{(\lambda_{\mathrm{m}}+2\mu_{\mathrm{m}})},\\
\lambda_{\mathrm{m}}&=\frac{v_{\mathrm{m}}E_{\mathrm{m}}}{(1+v_{\mathrm{m}})(1-2v_{\mathrm{m}})},\\
\mu_{\mathrm{m}}&=\frac{E_{\mathrm{m}}}{2(1+v_{\mathrm{m}})},
\end{aligned} \tag{8}$$

where E_{m} and v_{m} are the membrane Young's modulus and Poisson's ratio, respectively, and

$$S^{11}=E_{\mathrm{c}}G^{11}G^{11}E_{11} \tag{9}$$

for cables. Here E_{c} is the cable Young's modulus, G^{ij} are the components of the contravariant metric tensor in the undeformed coordinate system, and E_{kl} are the components of the Cauchy–Green strain tensor.

3. Finite element formulations

3.1. Fluid dynamics

To handle the time-variant spatial domains encountered in parachute problems, we employ the deforming-spatial-domain/stabilized space-time (DSD/SST) finite element formulation. This method has been applied to a large number of problems with moving boundaries and interfaces, and is well suited to handle the time-variant spatial domains.In order to construct the finite element function spaces for the space-time method, we partition the time interval $(0,T)$ into subintervals $I_n=(t_n,t_{n+1})$, where t_n and t_{n+1} belong to an ordered series of time levels $0=t_0<t_1<\cdots<t_N=T$. Let $\Omega_n=\Omega_{t_n}$ and $\Gamma_n=\Gamma_{t_n}$. We define the space-time slab Q_n as the domain enclosed by the surfaces Ω_n, Ω_{n+1}, and P_n, where P_n is the surface described by the boundary Γ_t as t traverses I_n. As it is the case with Γ_t, surface P_n is decomposed into $(P_n)_g$ and $(P_n)_h$ with respect to the type of boundary condition (Dirichlet or Neumann) being imposed. For each space-time slab, we define the corresponding finite element function spaces $(\mathscr{S}^h_{\mathbf{u}})_n$, $(\mathscr{V}^h_{\mathbf{u}})_n$, $(\mathscr{S}^h_p)_n$, and $(\mathscr{V}^h_p)_n$ Over the element domain, this space is formed by using first-order polynomials in space and time. Globally, the interpolation functions are continuous in space but discontinuous in time. The stabilized space-time formulation for deforming domains is then written as follows: given $(\mathbf{u}^h)_n^-$, find $\mathbf{u}^h\in(\mathscr{S}^h_{\mathbf{u}})_n$ and $p^h\in(\mathscr{S}^h_p)_n$ such that $\forall\mathbf{w}^h\in(\mathscr{V}^h_{\mathbf{u}})_n$ and $q^h\in(\mathscr{V}^h_p)_n$

$$\begin{aligned}
&\int_{Q_n}\mathbf{w}^h\cdot\rho\left(\frac{\partial\mathbf{u}^h}{\partial t}+\mathbf{u}^h\cdot\nabla\mathbf{u}^h+\mathbf{f}^h\right)\mathrm{d}Q+\int_{Q_n}\boldsymbol{\varepsilon}(\mathbf{w}^h):\boldsymbol{\sigma}(p^h,\mathbf{u}^h)\,\mathrm{d}Q+\int_{Q_n}q^h\nabla\cdot\mathbf{u}^h\,\mathrm{d}Q\\
&\quad+\sum_{e=1}^{n_{el}}\int_{Q_n^e}\frac{\tau}{\rho}\left[\rho\left(\frac{\partial\mathbf{w}^h}{\partial t}+\mathbf{u}^h\cdot\nabla\mathbf{w}^h\right)-\nabla\cdot\boldsymbol{\sigma}(q^h,\mathbf{w}^h)\right]\cdot\left[\rho\left(\frac{\partial\mathbf{u}^h}{\partial t}+\mathbf{u}^h\cdot\nabla\mathbf{u}^h+\mathbf{f}^h\right)-\nabla\cdot\boldsymbol{\sigma}(p^h,\mathbf{u}^h)\right]\mathrm{d}Q\\
&\quad+\sum_{e=1}^{n_{el}}\int_{Q_n^e}\delta\nabla\cdot\mathbf{w}^h\rho\nabla\cdot\mathbf{u}^h\,\mathrm{d}Q+\int_{\Omega_n}(\mathbf{w}^h)_n^+\cdot\rho\left((\mathbf{u}^h)_n^+-(\mathbf{u}^h)_n^-\right)\mathrm{d}\Omega=\int_{(P_n)_h}\mathbf{w}^h\cdot\mathbf{h}^h\,\mathrm{d}P.
\end{aligned} \tag{10}$$

This process is applied sequentially to all the space-time slabs $Q_0,Q_1,Q_2,\ldots,Q_{N-1}$. The computations start with $(\mathbf{u}^h)_0^-=\mathbf{u}_0$.

In the variational formulation given by Eq. (10), the first three terms and the right-hand side constitute the Galerkin formulation of the problem. The first series of element-level integrals in Eq. (10) are least-square terms based on the momentum equation. The second series of element-level integrals are added to the formulation for numerical stability at high Reynolds numbers. These are least-square terms based on the continuity of the equation. The stabilization coefficients τ and δ are defined at the element level. Both stabilization terms are weighted residuals, and therefore maintain the consistency of the formulation. Since the interpolation functions are discontinuous in time, the sixth term weakly enforces continuity of the velocity field across the space-time slabs.

3.2. Structural dynamics

A semi-discrete finite element formulation for the SD equations of motion is obtained from the principle of virtual work. Finite displacements of the structure are taken into account by using a Lagrangian description of the problem

$$\int_{\Omega_s^0} \rho^s \frac{\mathrm{d}^2\mathbf{y}}{\mathrm{d}t^2} \cdot \mathbf{w}\,\mathrm{d}\Omega + \int_{\Omega_s^0} \mathbf{S} : \delta\mathbf{E}(\mathbf{w})\,\mathrm{d}\Omega = \int_{\Gamma_s^t} \mathbf{t} \cdot \mathbf{w}\,\mathrm{d}\Gamma + \int_{\Omega_s^t} \rho^s \mathbf{f} \cdot \mathbf{w}\,\mathrm{d}\Omega. \tag{11}$$

Here the weighting function $\mathbf{w}$ is also the virtual displacement. The pressure contribution is included in the traction force $\mathbf{t}$ and increases the overall nonlinearity since it is a "follower force". The left-hand side terms of Eq. (10) are written in the original configuration and the right-hand side terms are written for the deformed configuration at time t. Upon discretization using appropriate function spaces, a nonlinear system of equations is obtained at each time-step and can be written in the incremental form as

$$\left(\frac{\mathbf{M}}{\beta\Delta t^2} + \frac{(1+\alpha)\gamma\mathbf{C}}{\beta\Delta t} + (1+\alpha)\mathbf{K}\right)\Delta\mathbf{y}^i = \mathbf{R}^i, \tag{12}$$

$$\mathbf{C} = \eta\mathbf{M} + \zeta\mathbf{K}. \tag{13}$$

Here $\mathbf{M}$ is the global mass matrix, $\mathbf{C}$ is a damping matrix for stabilization of the system, $\mathbf{K}$ is the stiffness matrix, $\mathbf{R}^i$ is the residual vector at the ith iteration, and $\Delta\mathbf{y}^i$ is the ith increment in the nodal displacements vector $\mathbf{y}$. The parameters α, β, γ arise from the Hilber–Hughes–Taylor [12] scheme which is used to advance the solution in time.

3.3. Mesh-moving strategy

An automatic mesh-moving scheme is used to handle the changing spatial domains encountered throughout the simulation. In this scheme, the fluid mesh is treated as a linearly elastic "pseudo-solid" that deforms as dictated by the motion of the surface boundaries of the fluid domain.

4. Fluid–structure coupling

The fluid–structure coupling is accomplished by communicating necessary information along the fluid–structure interface. For the problem addressed, the fluid–structure interface is represented by nodally equivalent interface meshes in the SD and FD models. Thus information is transferred between the SD and FD solutions in a node-for-node fashion. Surface displacements from the SD solution are treated as Dirichlet boundary conditions in the pseudo-solid formulation for the mesh moving scheme. Surface velocities from the SD solution are treated as Dirichlet boundary conditions in the DSD/SST formulation for the fluid. In return, parachute nodal surface pressures are applied as external forces on the structure in the SD formulation. It should be noted that the FD surface is doubly defined to account for distinct upper and lower surfaces, with the exception of the edges.

In a parachute FSI, the response of the parachute canopy to the surrounding flow field is severe. This strong response can impact the stability of numerically coupled simulations. Heavy mass-proportional damping has been imposed on the structural system to stabilize the solution. However, heavy mass-proportional damping significantly affects global behaviors and thus alters the dynamics of FSI solutions. For the problem presented, the SD surface velocities sent to the FD solver for treatment as boundary conditions have been "zeroed" in order to minimize the required amount of mass-proportional damping. Further work is focusing on methods for locally damping the structure without severely impacting global behaviors.

5. Test problem: 3-D FSI for a round parachute system

The Army's T-10 personnel parachute system is composed of a 35 foot diameter (D_c) canopy and 30 suspension lines each 29.4 feet long. The lines connect to two confluence points (which approximate the connection points for a personnel harness assembly). The canopy is called a "flat extended skirt canopy" because in its constructed (or nonstressed) configuration it is composed of a main circular section with a circular vent at the apex and an inverted flat ring section, which lies under the main section and is connected to the main section at the outer radius. The canopy lies flat as constructed and contains 30 gores. The suspension lines continue as 30 gore-to-gore reinforcements through the parachute canopy and meet at the apex. For the T-10, the extended skirt has a width which is 0.1 D_c and a vent diameter of 0.1 D_c. The cut-pattern for a single T-10 gore and the constructed configuration for the T-10 are shown in Fig. 1.

5.1. SD problem setup

The SD model mesh consists of 9183 nodes, 17 490 three noded membrane elements for the canopy surface, and 1920 two noded cable elements for the suspension lines and canopy reinforcements. This mesh results in 27 543 equations. The parachute system is represented by linearly elastic materials, which have properties and dimensions representative of a T-10. Fig. 2 shows a "blown out" view of the SD mesh for the main canopy reinforcements (cables), the main canopy (membranes), the extended skirt (membranes), and the extended skirt reinforcements and suspension lines (cables).

The model is allowed to inflate when the canopy is subjected to a prescribed differential pressure of 0.5 lb/ft^2. Fig. 3 shows the fully inflated static configuration for the T-10 model under the prescribed pressure loading. Maximum principal stresses for the parachute canopy (membrane) are superimposed on the surface, with low stresses (blue) along the canopy reinforcements and high stresses (red) in the midgore regions.

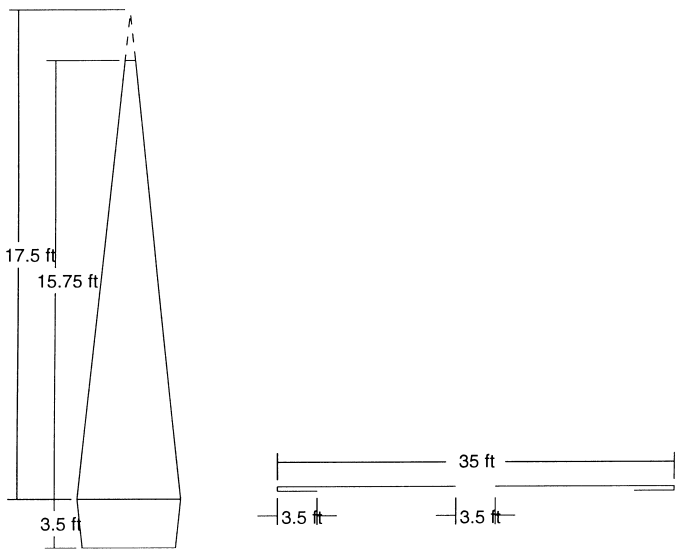

Fig. 1. T-1 gore and constructed configuration.

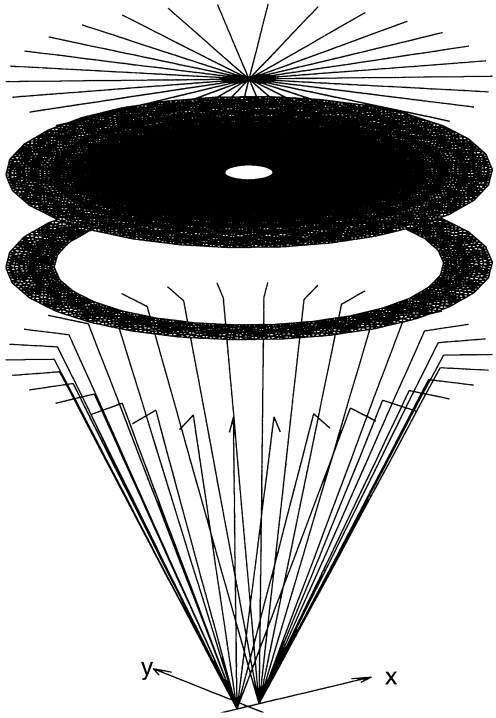

Fig. 2. T-10 SD model mesh.

Fig. 3. Fully inflated configuration for the T-10 model.

5.2. FD problem setup

A 3-D tetrahedral volume mesh was generated for the FD solution using as the surface mesh the three noded membrane mesh for the T-10 canopy in its inflated configuration. Canopy surface nodes were multiply defined, with one node for both the upper and lower surfaces. Thus, the fluid–structure interface (or T-10 canopy) is represented by nodally equivalent interface meshes. The mesh consists of 133 097 nodes and 783 910 tetrahedral elements, and results in 958 686 equations. Fig. 4 shows the surface mesh for the canopy and a slice of the 3-D mesh bisecting the canopy. Initial unsteady flow solutions were obtained for flow about the fixed canopy configuration at a Reynolds number of 10^7 using the space-time formulation. Fig. 5 shows a "snapshot" in time of the computed velocities and pressures for the flow field about the T-10 canopy.

The drag coefficient for parachutes is typically defined based on the constructed dimensions as follows:

$$C_{\mathrm{D}} = \frac{2D}{\rho V_t^2 S_0} \tag{14}$$

where D is the total drag, V_{t} is the terminal velocity of the parachute system, and S_0 is the total constructed area of the canopy. The average drag coefficient for the computed flow about the fixed canopy was 0.72 without accounting for suspension line drag contributions, payload drag contributions, or FSI effects. Experimental values for the T-10 parachute including drag contributions due to the payload and suspension lines range from 0.78 to 0.87. While the computed value for C_{D} correlates well with experiment, the terminal descent of a deformable parachute is governed by a FSI. Thus, it is necessary to obtain an average drag coefficient for the canopy as it interacts with the surrounding flow field.

5.3. FSI simulation

The FSI simulations are initiated using the fully inflated static configuration as the initial condition for the SD model, and the fully developed flow field about the fixed configuration as the initial condition for

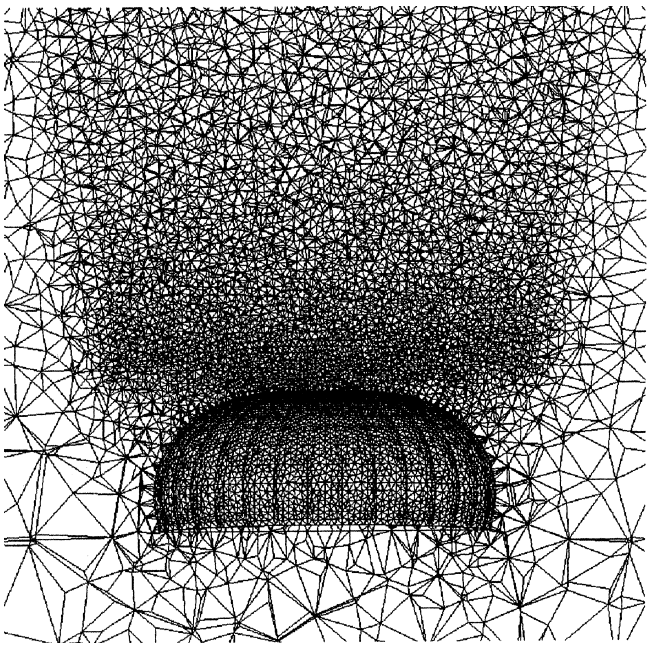

Fig. 4. T-10 canopy surface mesh and slice of 3-D mesh bisecting the canopy.

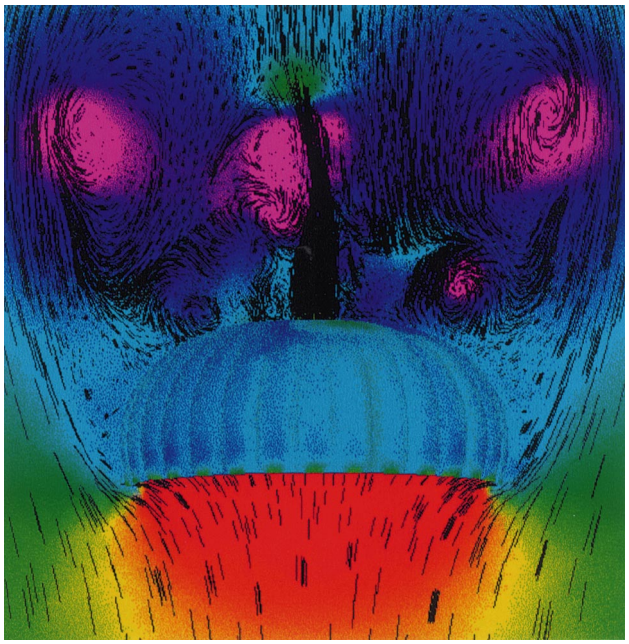

Fig. 5. Computed flow field about T-10 model.

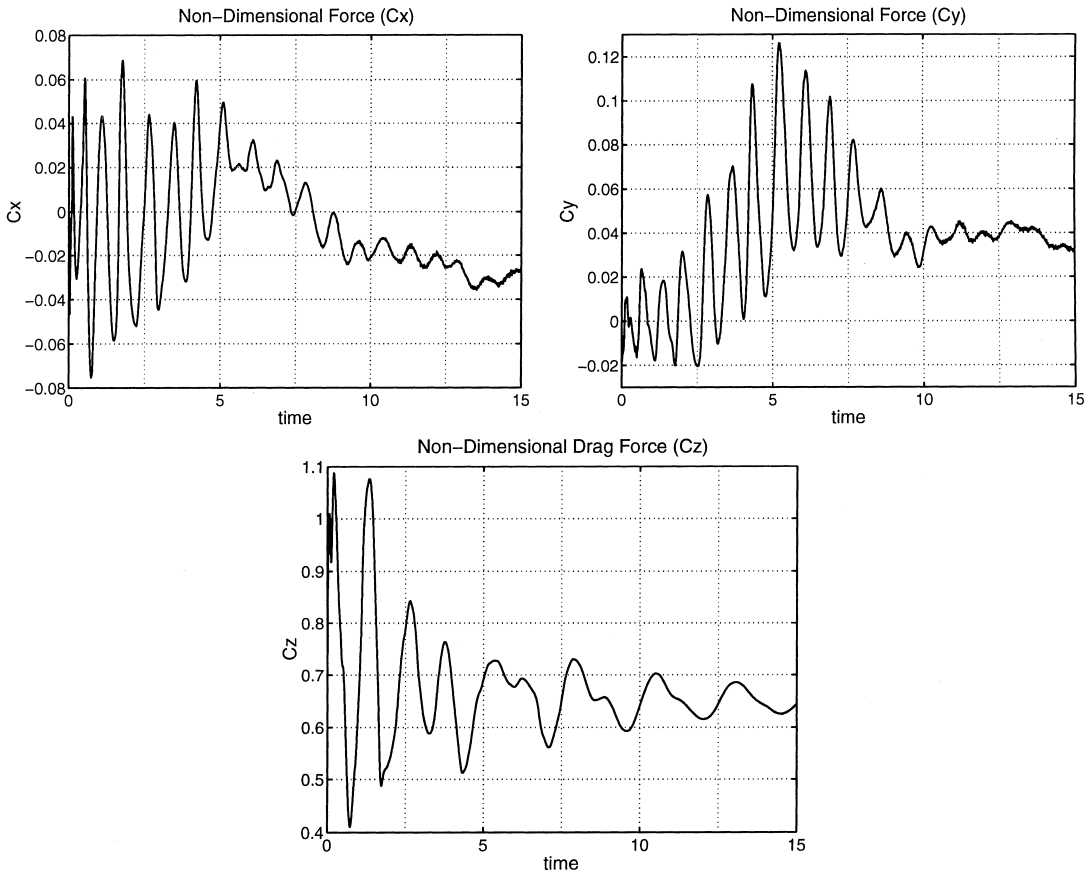

Fig. 6. Force histories.

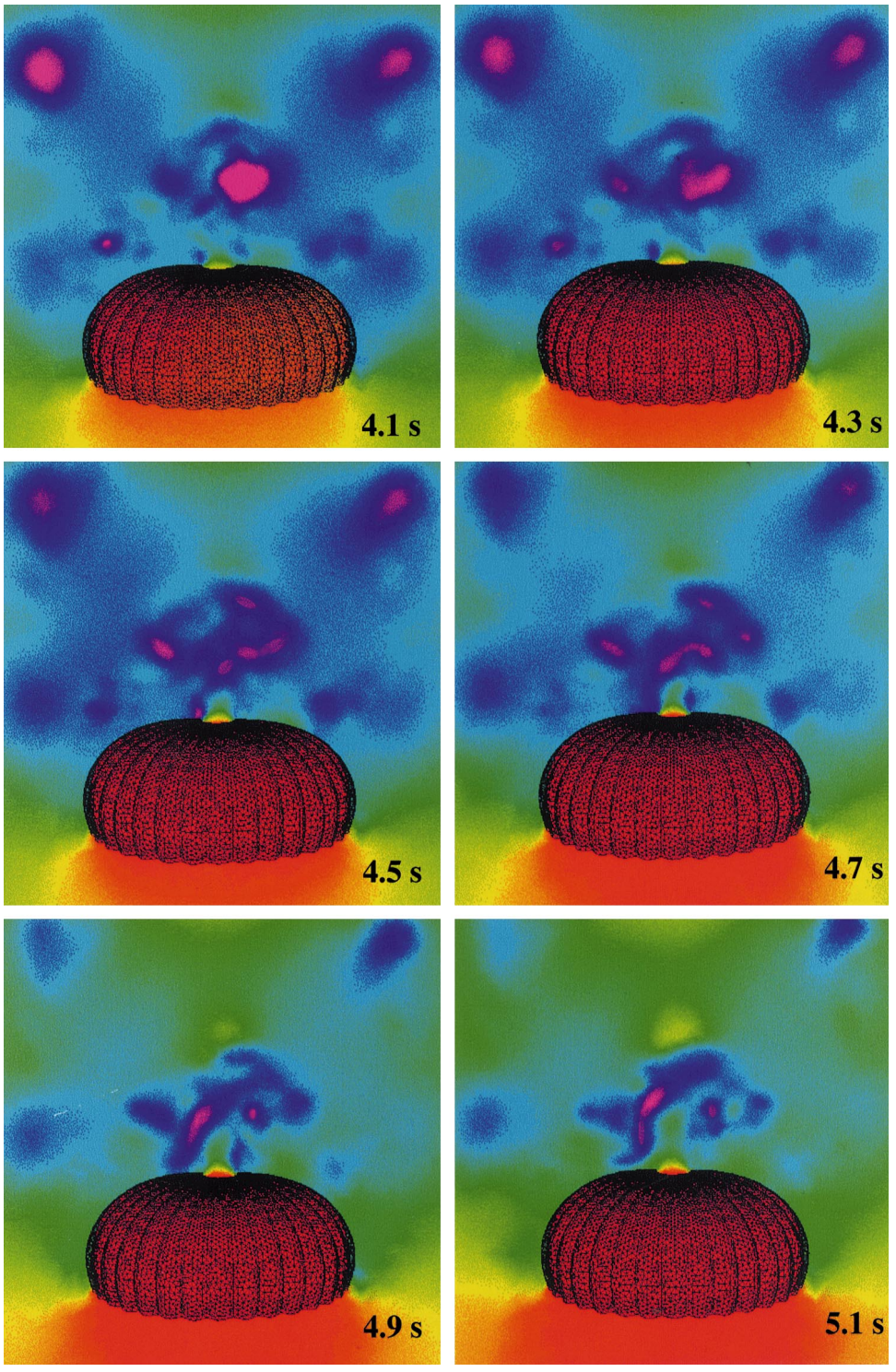

Fig. 7. Pressure: 4.1 to 5.1 s (red = high, magenta = low).

the flow field. All SD nodes were prescribed to have no initial velocities or accelerations. The two "payload" nodes in the SD model were fully constrained.

The coupled simulations were carried out with a time-step size of $\Delta t = 0.005$ s on the CRAY T3E-900 at Network Computing Services and on the CRAY T3E-1200 at the Army High Performance Computing

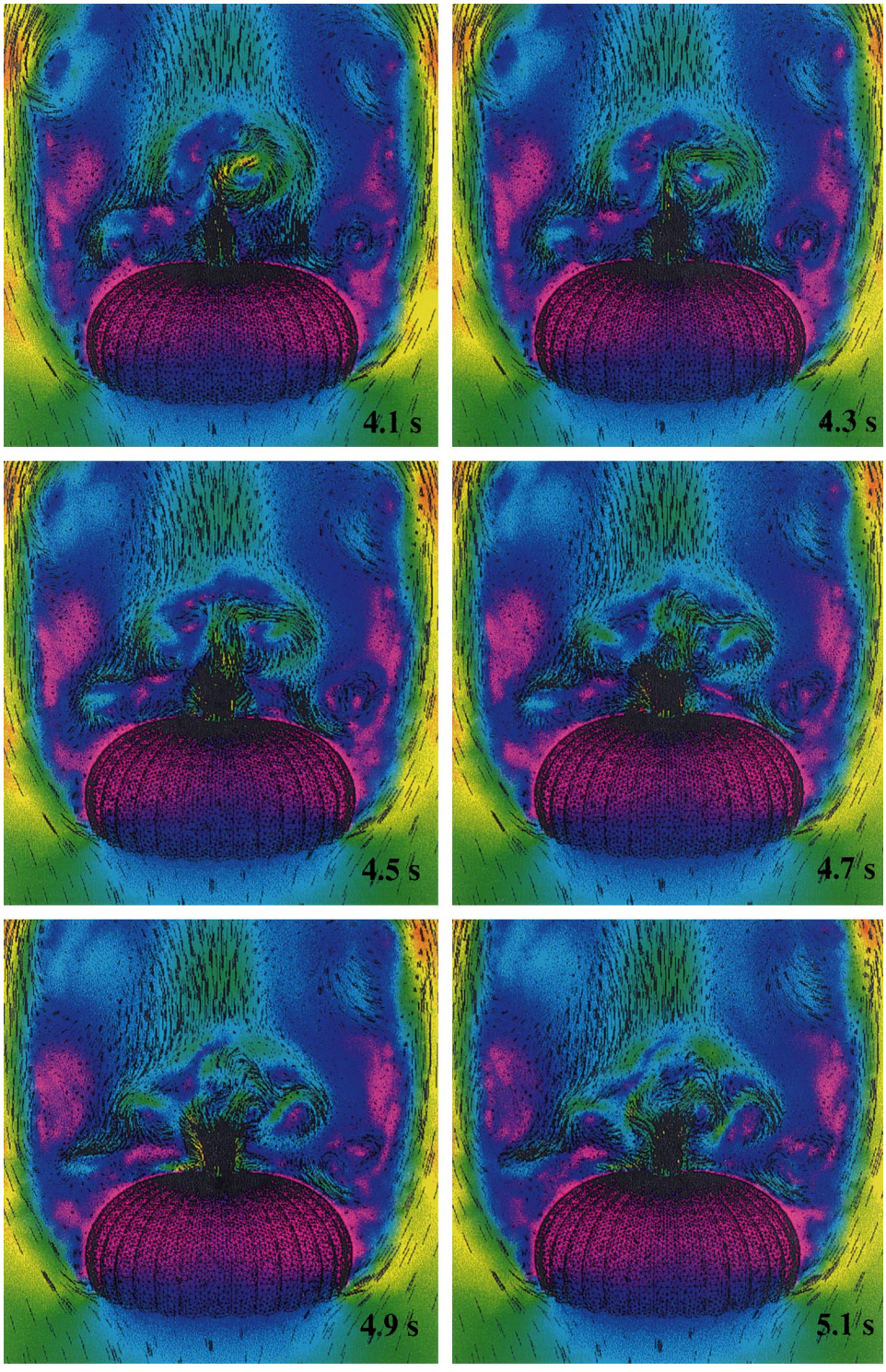

Fig. 8. Velocity magnitude: 4.1 to 5.1 s (red = high, magenta = low).

Research Center (AHPCRC). The aerodynamic force acting on the canopy was calculated at each time-step. Fig. 6 shows the time histories for each nondimensional force component. As in Eq. (13), the force terms are nondimensionalized based on the total constructed area of the canopy. The amplitude

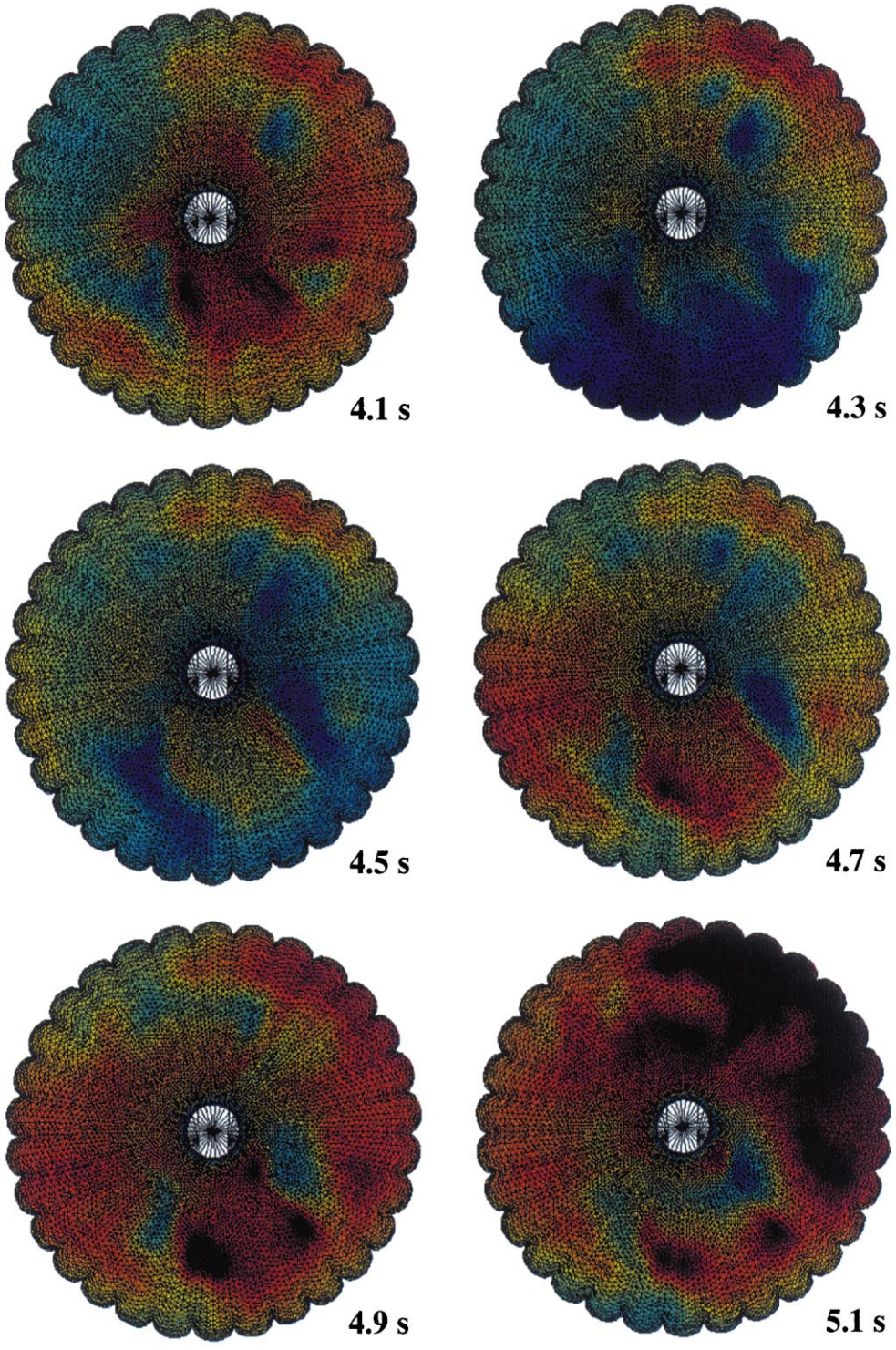

Fig. 9. Differential pressures on canopy: 4.1 to 5.1 s (red = high, blue = low).

of the oscillations is initially large due to the "relaxing" of the parachute structure from its initial configuration.

Figs. 7–10 show the time dependence of the FSI simulation from $t = 4.1$ s to $t = 5.1$ s in time intervals of 0.2 s. These snapshots represent a small subsample of the unsteady data in the FSI simulation, but they

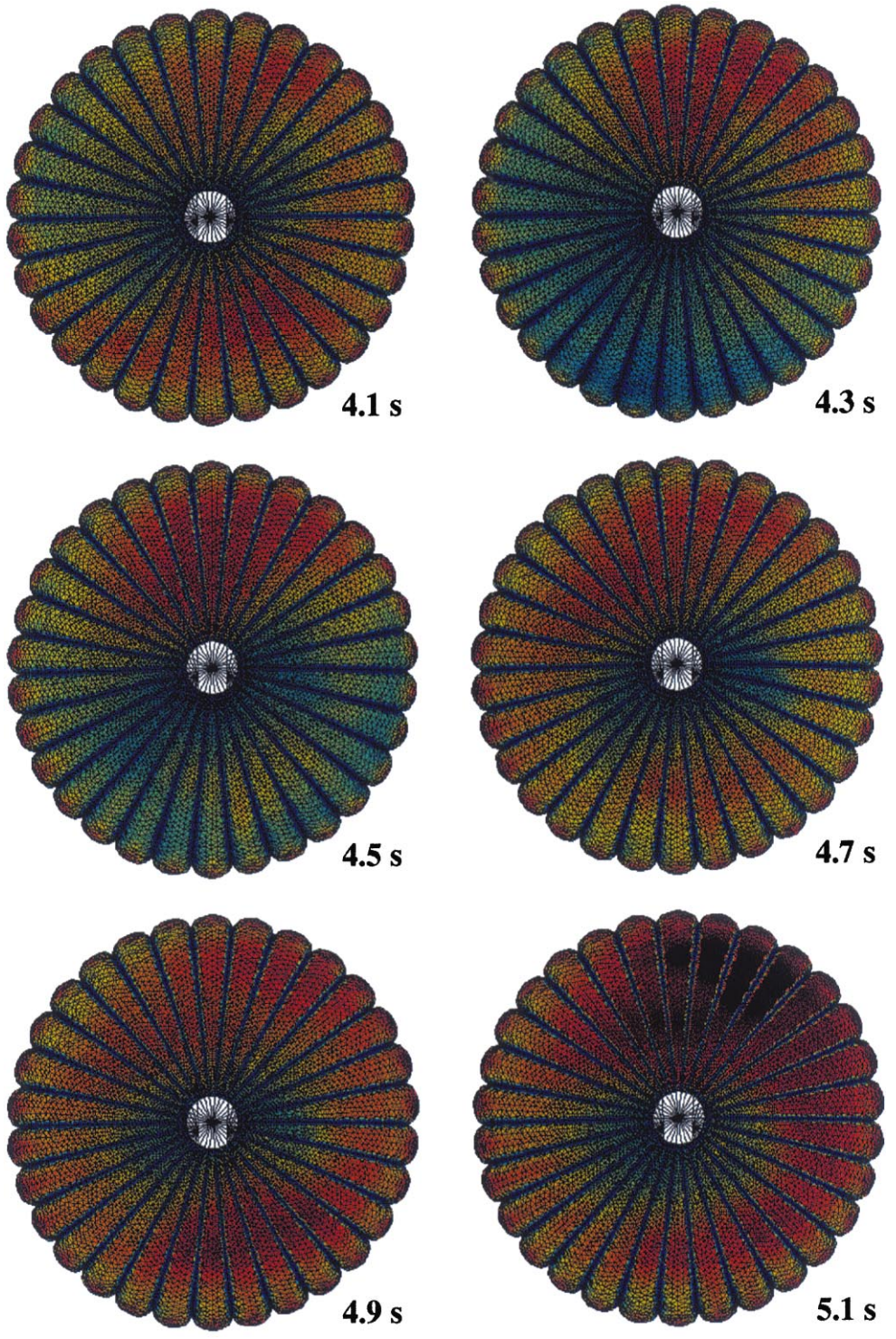

Fig. 10. Maximum principal stresses for canopy: 4.1 to 5.1 s (red = high, blue = low).

demonstrate the unsteadiness of the behavior. Figs. 7 and 8 show the time-dependent flow field surrounding the canopy in the $y = 0.0$ plane, which bisects the canopy in its initial configuration. Fig. 7 shows the computed pressure field $p/\rho V_\infty^2$ ranging from -0.8 (magenta) to 0.4 (red). Here V_∞ is the freestream velocity

in the FSI simulation. The wireframe mesh for the deforming canopy surface is shown superimposed in each frame.

Fig. 8 shows the computed velocity magnitude field $|\mathbf{v}|/V_\infty$ ranging from 0.0 (magenta) to 1.5 (red). The wireframe mesh for the deforming canopy surface is shown superimposed in each frame.

The dynamics of the parachute structure is shown in Figs. 9 and 10. Fig. 9 shows the computed differential pressure field $\Delta p/\rho V_\infty^2$ on the canopy surface. This is the pressure distribution from the FD computation, which is imposed as forces in the SD computation. Each frame is scaled consistently with blue and red corresponding to low and high differential pressures respectively. Differential pressure is defined positive outward for the upper canopy surface, and has values ranging from 0.21 to 1.20 for the frames shown.

Fig. 10 shows the computed maximum principal stresses for the canopy membranes, and are based on a thickness of 0.0001 ft for the undeformed membrane. Each frame is scaled consistently with blue and red corresponding to low and high stresses respectively. The stress values range from 16 to 20 575 $\mathrm{lb/ft^2}$ for the frames shown. Low stresses are experienced along canopy reinforcements and higher stresses are experienced in the canopy midgore regions. The canopy reinforcements that run radially through the canopy take up the majority of the overall load experienced by the T-10 parachute system.

6. Concluding Remarks

Parachute phenomena involve highly deformable structures interacting with complex flow fields. The ability to predict parachute phenomena requires the modeling of highly nonlinear FSI behaviors. This capability has only recently been attainable with advances in high performance computing methods and hardware. The US Army has accepted this challenge and this paper presents progress towards this goal. Historically, parachute development has been approached predominantly by expensive experimental methods. It is expected that further development of this capability will result in significant reduction of life cycle costs in the development of future airdrop systems.

This paper presents a methodology for carrying out simulations for parachute FSI that can be applied to a broad range of parachute applications. The FD model, SD model, and the coupling strategy undertaken have been described. A typical application "test problem" was presented to demonstrate this capability for a round parachute system. The test problem has shown the highly coupled behavior between the time-dependent flow field surrounding a round parachute and the dynamics of the parachute structure. Pressure and velocity distributions for the entire FD domain, including the canopy surface, were presented along with the time-dependent maximum principle stresses on the canopy membrane surface. A small subset of available data from postprocessing of the primary output of the simulation has also been presented. This includes the time dependent net forces on the parachute system. Details of stress histories in all structural components of the parachute system are extractable from the simulation results.

The capabilities presented in this paper have matured rapidly over the past few years, but more research is required to establish user friendly tools which could be used for parachute development. For example, the simulation presented has a fixed payload. Both the SD and FD software can be utilized in their current form to model a falling (completely unconstrained system). However, improvements in the boundary conditions imposed on the FSI surface and additional damping techniques to allow for this transition are needed and currently under development.

This work is continuing and a series of concurrent simulations, wind tunnel experiments and full scale drop tests are planned over the next two years to validate this parachute FSI simulation capability.

Acknowledgements

This work was sponsored in part by NASA-JSC (grant NAG9–919), ARO (grant DAAH04-93-G-0514), and by the Army High Performance Computing Research Center under the auspices of the Department of

the Army, Army Research Laboratory cooperative agreement number DAAH04-95-2-0003/contract number DAAH04-95-C-0008. The content does not necessarily reflect the position or the policy of the Government, and no official endorsement should be inferred. CRAY time was provided in part by the Minnesota Supercomputer Institute.

References

[1] C.W. Peterson, J.H. Strickland, H. Higuchi, The fluid dynamics of parachute inflation, Annual Review of Fluid Mechanics 28 (1996) 361–387.
[2] R.J. Benney, K.R. Stein, A computational fluid structure interaction model for parachute inflation, Journal of Aircraft 33 (1996) 730–736.
[3] V. Kalro, S. Aliabadi, W. Garrard, T. Tezduyar, S. Mittal, K. Stein, Parallel finite element simulation of large ram-air parachutes, International Journal for Numerical Methods in Fluids 24 (1997) 1353–1369.
[4] T.E. Tezduyar, M. Behr, J. Liou, A new strategy for finite element computations involving moving boundaries and interfaces – the deforming-spatial-domain/space-time procedure: I. The concept and the preliminary tests, Computer Methods in Applied Mechanics and Engineering 94 (1992) 339–351.
[5] T.E. Tezduyar, M. Behr, S. Mittal, J.Liou, A new strategy for finite element computations involving moving boundaries and interfaces – the deforming-spatial-domain/space-time procedure: II. Computation of free-surface flows, two-liquid flows, and flows with drifting cylinders, Computer Methods in Applied Mechanics and Engineering 94 (1992) 353–371.
[6] J. Smagorinsky, General circulation experiments with the primitive equations, Monthly Weather Review 91 (1963) 99–165.
[7] A.A. Johnson, T.E. Tezduyar, Parallel computation of incompressible flows with complex geometries, International Journal for Numerical Methods in Fluids 24 (1997) 1321–1340.
[8] R.J. Benney, K.R. Stein, J.W. Leonard, M.L. Accorsi, Current 3-D structural dynamic finite element modeling capabilities, in: Proceedings of the 14th AIAA Aerodynamic Decelerator Technology Conference, San Francisco, 1997.
[9] N. Maman, C. Farhat, Matching fluid and structure meshes for aeroelastic computations: a parallel approach, Computers and Structures 54 (1995) 779–785.
[10] A.A. Johnson, T.E. Tezduyar, Mesh update strategies in parallel finite element computations of flow problems with moving boundaries, Computer Methods in Applied Mechanics and Engineering 119 (1994) 73–94.
[11] K.R. Stein, R.J. Benney, V. Kalro, A.A. Johnson, T.E. Tezduyar, Parallel computation of parachute fluid–structure interactions, in: Proceedings of the 14th AIAA Aerodynamic Decelerator Technology Conference, San Francisco, 1997.
[12] H.M. Hilber, T.J.R. Hughes, R.L. Taylor, Improved numerical dissipation for time integration algorithms in structural dynamics, Earthquake Engineering and Structural Dynamics 5 (1977) 283–292.